Heterogeneous Catalysts

Deutsche Ausgabe: DOI: 10.1002/ange.201907117
Internationale Ausgabe: DOI: 10.1002/anie.201907117

Oxidation of Reduced Ceria by Incorporation of Hydrogen

Zhaorui Li[+], Kristin Werner[+], Kun Qian[+], Rui You, Agata Płucienik, Aiping Jia, Lihui Wu, Liyuan Zhang, Haibin Pan, Helmut Kuhlenbeck, Shamil Shaikhutdinov, Weixin Huang und Hans-Joachim Freund**

Abstract: *The interaction of hydrogen with reduced ceria (CeO_{2-x}) powders and CeO_{2-x}(111) thin films was studied using several characterization techniques including TEM, XRD, LEED, XPS, RPES, EELS, ESR, and TDS. The results clearly indicate that both in reduced ceria powders as well as in reduced single crystal ceria films hydrogen may form hydroxyls at the surface and hydride species below the surface. The formation of hydrides is clearly linked to the presence of oxygen vacancies and is accompanied by the transfer of an electron from a Ce^{3+} species to hydrogen, which results in the formation of Ce^{4+}, and thus in oxidation of ceria.*

Introduction

Hydrogen adsorption and dissociation on metal oxides are of great importance both fundamentally and industrially.[1] Two mechanisms for H_2 dissociation on metal oxide surfaces have been identified:[2] One is the homolytic dissociation, which produces two hydrogen atoms at two oxygen sites, leading to the formation of two OH groups and the concomitant reduction of two surface metal ions; the other one is the heterolytic (polar) dissociation, which entails the formation of a hydride, H^-, and a proton, H^+, at metal and oxygen sites, yielding M-H and OH species, respectively. The H ad-atoms on metal oxide surfaces can migrate into the subsurface region and further into the bulk to form hydroxyl and hydride species therein. As demonstrated by experimental and theoretical studies,[3] the general trend is that heterolytic cleavage occurs on oxides which are difficult to reduce, such as MgO,[4] Al_2O_3,[5] and SiO_2,[6] whereas homolytic cleavage at two oxygen sites is thermodynamically favored for readily reducible oxides such as TiO_2 and CeO_2.[7] However, heterolytic cleavage of H_2 was also reported for readily reducible oxides, such as Ga_2O_3,[8] Cr_2O_3,[9] ZnO,[10] and TiO_2.[11] On the latter, defects were observed to play a key role in stabilizing the hydride species. We demonstrate here, that in the presence of defects in ceria leading to a reduction of ceria and thus to the formation of Ce^{3+} species, hydrogen incorporation below the surface may trigger the formation of hydride species by transferring the 4f electron at a Ce^{3+} center to a hydrogen atom, which then occupies the oxygen vacancy.

Ceria (CeO_2) has recently been studied as a selective catalyst in the partial hydrogenation of alkynes to alkenes,[12] which inspired strong interest in revisiting the H_2-ceria interaction. DFT calculations have suggested that the stoichiometric CeO_2 surface kinetically favors the heterolytic dissociation of H_2 to form Ce–H and OH species, and that the resulting Ce–H further evolves to the thermodynamically more stable OH species, accompanied with the reduction of Ce^{IV} to Ce^{III}.[12f,13,29] It was further reported that the presence of surface oxygen vacancies (Vo) on ceria not only facilitates the heterolytic dissociation of H_2, but also enhances the stability of Ce-H hydride species.[12i,14] Experimentally, surface oxygen vacancies on ceria were found to locally affect the reactivity of surface hydroxyl groups: While recombinative desorption as water is suppressed at high oxygen vacancy density, the production of H_2 is favored.[15] Recently, the first direct spectroscopic evidence for the presence of both surface and bulk Ce-H species upon H_2 dissociation over defect-rich ceria nanorods was provided via in situ inelastic neutron scattering spectroscopy.[16] Furthermore, H_2 dissociation on a thin CeO_2(111) film on Ru(0001) was observed at H_2 pressures in the mbar regime.[17] The resulting H species stay on the surface of stoichiometric CeO_2(111), whereas H incorporation below the surface occurs on partially reduced CeO_{2-x}(111) ($x \approx 0.1$–0.2). A reaction channel with bulk CeO_{2-x} has recently also been identified for the incorporation of hydroxyls.[18]

[*] Z. Li,[+] Dr. K. Qian,[+] Dr. R. You, A. Jia, L. Zhang, Prof. Dr. W. Huang
Hefei National Laboratory for Physical Sciences at Microscale, Key Laboratory of Surface and Interface Chemistry and Energy Catalysis of Anhui Higher Education Institutes, CAS Key Laboratory of Materials for Energy Conversion and Department of Chemical Physics, University of Science and Technology of China
Hefei 230029 (China)
E-Mail: huangwx@ustc.edu.cn

K. Werner,[+] A. Płucienik, Dr. H. Kuhlenbeck, Dr. S. Shaikhutdinov, Prof. Dr. H.-J. Freund
Fritz-Haber-Institut der Max-Planck-Gesellschaft
Faradayweg 4–6, 14195 Berlin (Germany)
E-Mail: freund@fhi-berlin.mpg.de

A. Jia
Key Laboratory of the Ministry of Education for Advanced Catalysis Materials, Institute of Physical Chemistry Zhejiang Normal University, Jinhua 321004 (China)

Dr. L. Wu, Dr. H. Pan
National Synchrotron Radiation Laboratory, University of Science and Technology of China, Hefei 230029 (China)

[+] These authors contributed equally to this work.

Supporting information and the ORCID identification number(s) for the author(s) of this article can be found under https://doi.org/10.1002/anie.201907117.

In this paper, we discuss H_2 adsorption on reduced ceria surfaces (CeO_{2-x} powder and CeO_{2-x}(111) thin films) at different pressures and adsorption temperatures. The combination of studies on atomically well-defined CeO_{2-x}(111) thin films and morphologically complex CeO_{2-x} powder allows us to extract information on chemical processes on a model thin film and to verify their relevance on a realistic powder system. Our experiments reveal that reduced ceria is oxidized upon H_2 adsorption, which provides further evidence for a novel type of H_2 dissociation on ceria to form hydrides at oxygen vacancies. The results are presented in two parts: The first part summarizes the evidence for oxidation of reduced ceria upon hydride formation, taking into account both powder and single crystal thin film experiments, while the second part provides additional information on powder samples.

Results and Discussion

The structure of the ceria samples has been characterized by standard techniques, that is, by transmission electron microscopy (TEM) and X-ray diffraction (XRD) for the powder samples, and low energy electron diffraction (LEED) for the single crystal thin films. The ceria powder consists of 20–50 nm large nanoparticles with irregular polyhedral or spherical shapes that show (111) lattice fringes of cubic fluorite CeO_2 (Figure S1). CeO_2 thin films exhibit (111) orientation and show a well-resolved hexagonal LEED pattern under ultrahigh vacuum (UHV) conditions (Figure S2). Some reduced CeO_{2-x}(111) films faintly show the $\sqrt{7} \times \sqrt{7}$ structure of $CeO_{1.71}$(111) (Figure S2), as previously reported and analyzed by scanning probe and diffraction studies.[19] CO titration experiments showed that the stoichiometric CeO_2(111) film as well as the reduced CeO_{2-x}(111) film are continuous and that only a negligible fraction of the Ru substrate is exposed. Using XPS in a series of annealing experiments, we found that both films are thermally stable in UHV up to at least 1000 K.

Figure 1 A a shows Ce 3d and O 1s X-ray photoelectron spectroscopy (XPS) results of the freshly prepared CeO_{2-x}-(111) thin film. Spectra where recorded in both normal ($\theta = 0°$) and grazing (surface-sensitive) emission geometry ($\theta = 60°$), which differ in the angle θ between surface normal and XPS analyzer. We estimate that 95% of the electrons in the Ce 3d region originate from the topmost ≈ 35 Å (≈ 17 Å) of the thin film in normal (grazing) emission.[20] The Ce 3d XP spectrum shows characteristic peaks of Ce^{4+} species in three doublets, as well as of Ce^{3+} species in two additional doublets.[19b,21] The applied XPS peak fitting parameters and peak positions are described in detail in the Supporting Information. The relative Ce^{3+} concentration was calculated as the ratio of Ce^{3+} peak area over the whole Ce 3d region, that is, $A(Ce^{3+})/[A(Ce^{3+}) + A(Ce^{4+})]$. We estimate that the maximum error of this procedure, due to the complexity of the Ce 3d spectrum and the uncertainty of the Shirley background, does not exceed $\pm 10\%$.[19b,21] With this, we estimate the Ce^{3+} concentration as 6% within the topmost 35 Å and 17% within the topmost 17 Å. This indicates that the concentration of Ce^{3+} species is larger close to the surface as compared to deeper layers. The O 1s XP spectrum for fresh CeO_{2-x}(111) shows a main peak at 529.8 eV with a shoulder at 531.8 eV, originating from O^{2-} ions and surface OH groups, respectively.[22] The presence of hydroxyl species (in a comparably low density) can be explained by the dissociative adsorption of water (from the UHV background) over surface oxygen vacancies.[15a]

Figure 1 B a shows normal emission Ce 3d and O 1s XP spectra of pretreated CeO_{2-x} powder (heated to 773 K for 30 min in UHV). Ce 3d XP spectra were fitted with Ce^{3+} and Ce^{4+} components according to previously well-established procedures.[23] The employed peak fitting procedure of Ce 4f XPS spectra of CeO_2 powders gave the maximum error of $\pm 11\%$. The powder exhibits a Ce^{3+} concentration of 9.2% within the topmost ≈ 35 Å, which indicates the presence of surface oxygen vacancies.[20] The O 1s XP spectrum shows a main peak at 529.1 eV, originating from O^{2-} ions, and two shoulders at 531.0 and 533.5 eV, corresponding to surface OH

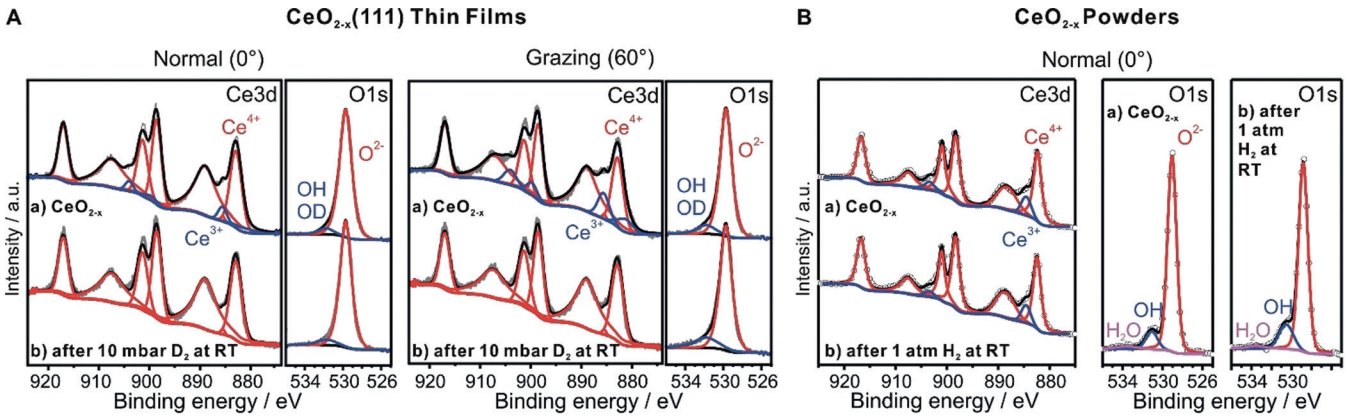

Figure 1. A) Ce 3d and O 1s XP spectra of CeO_{2-x}(111) thin film in normal (0°) and grazing (60°) emission geometry: a) Freshly prepared CeO_{2-x}(111), b) CeO_{2-x}(111) exposed to 10 mbar D_2 at 300 K. B) Ce 3d XP and O 1s XP spectra of CeO_{2-x} powder before (a) and after (b) exposure to 1 atm H_2 at 303 K.

groups (concentration 10.2%) and adsorbed water (3.5%), respectively.[22] The presence of both species results from the adsorption of water from the UHV background. The much higher concentration of hydroxyl species on the CeO_{2-x} powder as compared to the CeO_{2-x}(111) film, together with the presence of adsorbed water only on CeO_{2-x} powder, suggest that the CeO_{2-x} powder is more defective than the CeO_{2-x}(111) film. In addition, surface-sensitive valence band photoelectron spectra of CeO_{2-x} powder (Figure S3) were obtained at photon energies of 124.5, 122, and 115 eV. These energies correspond to on-resonance Ce^{4+} and Ce^{3+} 4d-4f excitation and off-resonance excitation, respectively. We estimate that 95% of the photoelectrons in the valence band spectra originate from the topmost layers ($\approx$15 Å) of the ceria powder.[20] The calculated Ce^{3+} concentration of pretreated CeO_{2-x} powder (heated to 773 K for 30 min in UHV) is 50.9%, hence much higher than estimated from the Ce 3d XPS data. The increased value obtained from the surface-sensitive valence band measurements indicates that Ce^{3+} is enriched in the near-surface region of the pretreated CeO_{2-x} powder. This observation is consistent with the results on the CeO_{2-x}(111) thin film. We assume the concentration gradient of Ce^{3+} in both systems to follow that of oxygen vacancies from the surface (high concentration) towards deeper layers (lower concentration), since the formation of oxygen vacancies results in the reduction of Ce^{4+} species to Ce^{3+} in close proximity.[24] Such a gradient in oxygen vacancy concentration has been observed before on related systems, such as CeO_{2-x}-(111) thin films[19b,c] and islands.[25]

Figures 1 A b and B b, respectively, show the electronic structure of reduced CeO_{2-x}(111) and CeO_{2-x} powder upon interaction with molecular hydrogen. The clean CeO_{2-x}(111) thin film was exposed to 10 mbar D_2 at 300 K for 15 min. Under similar experimental conditions, we previously observed negligible surface OH formation and incorporation of H species below the CeO_{2-x}(111) surface.[17] Figure 1 A b shows Ce 3d and O 1s XP spectra obtained after D_2 exposure. In the Ce 3d spectra, the Ce^{3+} concentration significantly decreases after 10 mbar D_2 exposure in both normal and grazing emission modes. The total peak area of Ce species, however, remains unchanged, which demonstrates that part of the Ce^{3+} species are transformed to Ce^{4+}. Furthermore, the Ce:O stoichiometry of the film remains unchanged. The O 1s region shows a slight increase in OD signal (with respect to all O species), while the overall peak area of all O species stays unchanged within the experimental error margin. This suggests the formation of OD groups in small density. The absence of other clear signals in the O region indicates that the sample, even after exposure to 10 mbar of D_2, is largely free from contaminants like adsorbed water or carbonates. These findings demonstrate that through exposure to D_2, Ce^{3+} in CeO_{2-x}(111) films may be oxidized to Ce^{4+}. This phenomenon occurs both in surface-near and deeper layers.

The CeO_{2-x} powder was exposed to 1 atm H_2 at 303 K for 1 h. Subsequently measured Ce 3d and O 1s XP spectra are shown in Figure 1 B b. The total peak areas of Ce species and O species, as well as the O/Ce ratio remain unchanged after H_2 treatment (Figure S4). The Ce^{3+} concentration decreases from 9.2% to 6.5%, which implies hydrogen adsorption-induced oxidation. Such an oxidation phenomenon can be clearly seen by a direct comparison of Ce 3d XP spectra of CeO_{2-x} powder before and after the exposure to 1 atm H_2 at 303 K (Figure S5). This agrees with the results obtained on the CeO_{2-x}(111) thin film. The less extensive oxidation of CeO_{2-x} powder upon H_2 treatment as compared to the CeO_{2-x}(111) thin film may arise from the pronounced morphological differences between powder and single crystal surfaces, and especially from a higher density of defects on the powder sample. The O 1s XP spectrum shows that the OH concentration increases from 10.2% to 15.1% after H_2 treatment, while the concentration of adsorbed water decreases slightly from 3.5% to 3.0%. The increase of OH density implies that H_2 dissociates on the powder surface at 303 K to form OH species, which is expected to increase the Ce^{3+} concentration:[13b,15a,26]

$$H_2 + 2O^{2-} + 2Ce^{4+} \rightarrow 2OH^-_{ads} + 2Ce^{3+} \quad (1)$$

The changes in Ce^{3+} concentration in the CeO_{2-x} powder upon H_2 treatment were also examined by Electron Spin Resonance (ESR) spectroscopy (Figure 2). ESR is a Ce^{3+}-sensitive technique, which probes both the surface and the bulk of ceria. Before exposure to H_2, the CeO_{2-x} powder shows a Ce^{3+} ESR feature at $g_\perp$ of 1.967 and $g_\parallel$ of 1.940,[27] suggesting the presence of oxygen vacancies. Further observed features, which are apparent also for the as-received powder (Figure S6), are typical of nuclei with I = 5/2.[28] We tentatively attribute these signals to unreactive impurities. After H_2 exposure (1 atm, 303 K, 1 h), the Ce^{3+} ESR feature weakens significantly to 17% of the ESR signal before exposure. In agreement with the XPS data, these ESR results clearly imply the oxidation of Ce^{3+} to Ce^{4+} by H_2 treatment at 303 K. Since the ESR measurement probes a larger depth than XPS, we conclude that oxidation of Ce^{3+} readily occurs also in deeper layers.

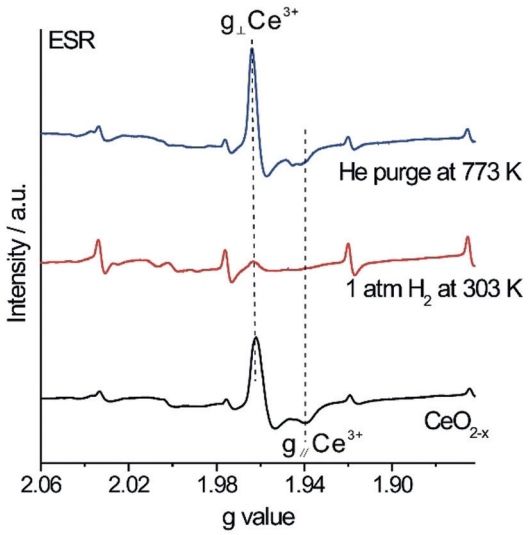

Figure 2. ESR spectra of CeO_{2-x} powder before and after exposure to 1 atm H_2 at 303 K, and after subsequent purging in He at 773 K.

The oxidation of the CeO_{2-x}(111) thin film upon H_2 exposure at 300 K is further confirmed by electron energy loss spectroscopy (EELS) of valence electron excitations across the band gap with loss energies up to 10 eV (Figure 3). The EEL spectra of CeO_2(111) and CeO_{2-x}(111) films are

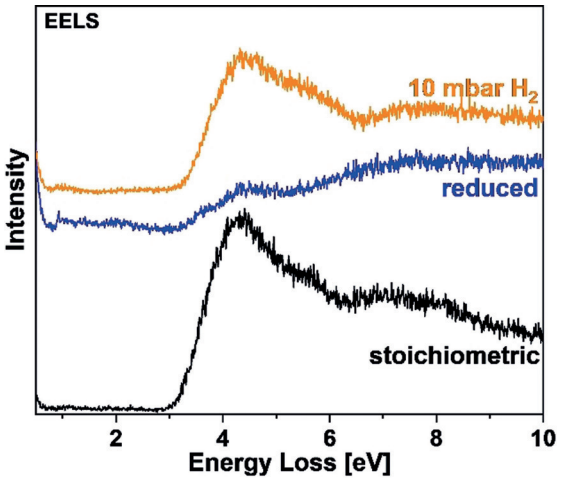

Figure 3. EELS spectra of differently prepared CeO_2(111) thin film surfaces. Reduction of CeO_2(111) to CeO_{2-x}(111) was achieved by annealing in UHV. The reduced CeO_{2-x}(111) film was then exposed to 10 mbar H_2 at 300 K for 15 min. The spectra were recorded in sequence from the bottom to the top.

similar to those reported by Pfau and Schierbaum.[29] The optical band gap of CeO_2 with a width of ≈3.5 eV[26] gives rise to the flat area below ≈3 eV, and the structures in the spectrum of stoichiometric CeO_2(111) are all due to transitions from the O 2p valence band to empty cerium states. In the case of reduced CeO_{2-x}(111), additional transitions with Ce 4f initial states arise. Reduction has a massive effect on the spectrum of the ceria surface, since it modifies the local electronic structure and is expected to change the local geometry. After exposure of the reduced CeO_{2-x}(111) film to 10 mbar H_2 at 300 K, the spectrum becomes very similar to that of the stoichiometric CeO_2(111) surface, although the observed features are somewhat weaker. This indicates that the resulting H species within the CeO_{2-x}(111) film can restore the valence band structure to that of the stoichiometric surface. This does not only demonstrate that H_2 adsorption induces oxidation of Ce^{3+} to Ce^{4+}, but also that it re-establishes the atomic structure of the stoichiometric surface, since the valence band structure depends sensitively on the atomic positions. In addition to transitions from the O 2p initial states, the spectrum of the hydrogenated film should also include transitions from H 1s initial states. These features, however, are rather weak in intensity, and are hidden below the regular CeO_2 transitions.

The electronic changes that occur upon H_2 adsorption on reduced ceria powder and CeO_{2-x}(111) thin films clearly demonstrate a H_2-induced oxidation at 300 K, which constitutes a novel interaction of hydrogen with reduced ceria. Charge transfer from Ce^{3+}/oxygen vacancy sites to H species oxidizes Ce^{3+} to Ce^{4+}. We thus propose that H may be stabilized as a hydride (Ce^{4+}-H^-) at these sites. The oxidation of reduced ceria takes place in near-surface regions, as well as in the ceria bulk. An apparent difference between the experiments on CeO_{2-x}(111) thin films and CeO_{2-x} powder is that H_2 exposure leads to a full oxidation of CeO_{2-x}(111), while CeO_{2-x} powder is partially oxidized. We attribute this difference to the dissimilarities in morphological structure between the two systems, that is, the presence of non-(111) oriented facets, a higher density of structural surface defects, and potential impurities on the CeO_{2-x} powder.

Furthermore, we investigated the thermal stability of Ce^{4+}-H^- hydride species within CeO_{2-x} powder and CeO_{2-x}-(111) thin films. We flashed the 10 mbar D_2-exposed CeO_{2-x}-(111) thin film in UHV stepwise to elevated temperatures and recorded grazing emission Ce 3d XP spectra in between heating steps (Figure S7). A plot of the relative Ce^{3+} concentration versus flashing temperature (Figure 4 A) shows

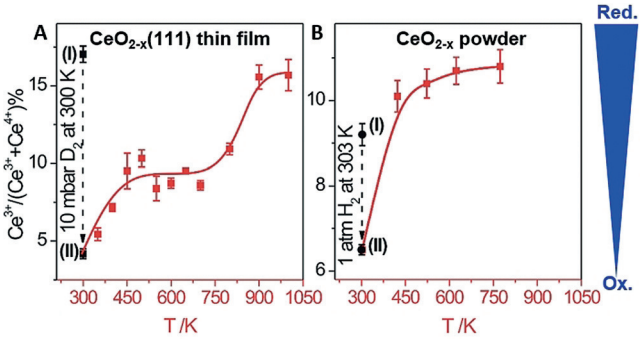

Figure 4. Ce^{3+} concentration in CeO_{2-x} before and after H_2 treatment and subsequent (stepwise) heating: A) CeO_{2-x}(111) thin films before (I) and after (II) D_2 exposure (10 mbar, 15 min, 300 K) and subsequent flashing to indicated temperatures. Ce^{3+} concentration evaluated from grazing emission Ce 3d XPS. B) CeO_{2-x} powder before (I) and after (II) H_2 exposure (1 atm, 1 h, 303 K) and subsequent annealing at indicated temperatures (1 h for $T > 303$ K). Ce^{3+} concentration evaluated from normal emission Ce 3d XPS.

that the oxidation state of CeO_{2-x}(111) is recovered in two steps. Partial recovery of Ce^{3+} takes place at $T < 450$ K, while almost complete recovery happens above 800 K. O 1s spectra (not shown) indicate that the O concentration remains unchanged after flashing to 1000 K, which verifies that the distribution of O species in the film is not related to the change in oxidation state.

In a similar experiment, 1 atm H_2-exposed CeO_{2-x} powder was annealed at elevated temperatures for 1 h in UHV, and normal emission XP spectra were acquired in between annealing steps (Figure S8). The relative concentration of Ce^{3+} as a function of the annealing temperature is shown in Figure 4 B. Upon annealing at 423 K, the Ce^{3+} concentration rises from 6.5 % to 10.1 %, which is higher than the original concentration on the ceria powder before H_2 exposure (9.2 %). With increasing annealing temperature, the Ce^{3+} concentration furthermore increases slightly, and finally reaches 10.8 % upon annealing at 773 K. Similarly, when the H_2-exposed CeO_{2-x} powder is purged in He at 773 K for 1 h, ESR (see Figure 2) shows an increase in Ce^{3+} concentration to

120% with respect to the CeO_{2-x} powder before H_2 treatment. We relate the clear increase of Ce^{3+} concentration upon annealing to the disappearance of Ce^{4+}-H^- hydride species, which recovers Ce^{3+}/oxygen vacancy sites. The increase in Ce^{3+} concentration to values above the original Ce^{3+} concentration before H_2 exposure, as observed in both XPS and ESR measurements, may be explained by H_2 dissociation to form surface hydroxyls and eventually water, which results in reduction of Ce^{4+} to Ce^{3+}.

In order to verify that indeed the disappearance of hydride species results in the recovery of Ce^{3+}, we followed desorption from the ceria powder by thermal desorption spectroscopy (TDS).

Figure 5 shows H_2O and H_2 TDS curves of CeO_{2-x} powder before and after H_2 treatment and subsequent He purging at 303 K. H_2O desorbs from the unexposed CeO_{2-x} powder in

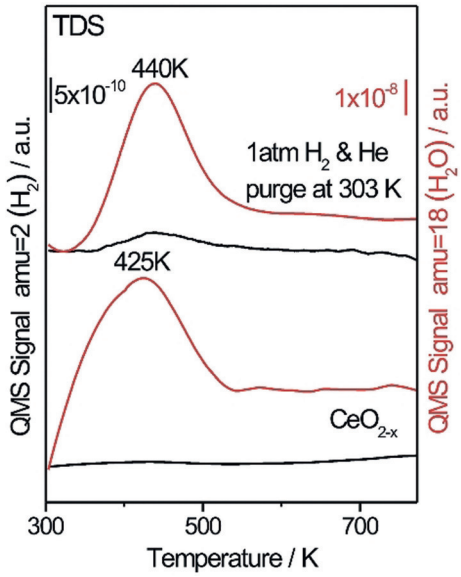

Figure 5. H_2 (black) and H_2O (red) TDS spectra of CeO_{2-x} powder before (bottom) and after exposure to 1 atm H_2 at 303 K and subsequent purging in He at 303 K (top).

a broad desorption feature at 425 K, which arises from recombinative desorption of surface hydroxyl groups and desorption of molecularly adsorbed water.[15b] Both species originate from adsorption of residual water on the CeO_{2-x} powder. No desorption of H_2 is observed. After exposure to 1 atm H_2 and subsequent purging at 303 K, the TDS curves show a similar symmetric H_2O desorption peak at 440 K with a very weak high-temperature shoulder up to 700 K, caused by recombinative desorption of surface hydroxyls.[15a] Meanwhile, H_2 desorbs from the H_2-exposed ceria powder at 440 K, hence in the same temperature range where recovery of Ce^{3+} was observed by XPS. To exclude that the observed desorption of H_2 at 440 K is related to desorption of surface hydroxyls, we followed their concentration by O 1s XPS in between annealing steps. Figure 6 shows the concentration of hydroxyl groups on the CeO_{2-x} powder before and after H_2 treatment and subsequent annealing. The OH concentration remains approximately unchanged upon annealing to 523 K,

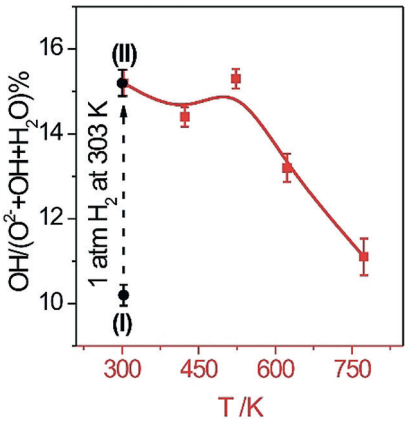

Figure 6. OH concentration on CeO_{2-x} powder before (I) and after H_2 treatment (1 atm, 1 h, 303 K) and subsequent (stepwise) annealing (1 h at indicated temperature for $T > 303$ K) (II). OH concentration evaluated from normal emission O 1s XPS.

and decreases only with further annealing at 623 K and 773 K. Hydroxyl groups hence desorb from the ceria powder at $T > 523$ K, that is, at temperatures higher than where H_2 desorption and most pronounced recovery of Ce^{3+} species are observed. We therefore conclude that these phenomena are not related to desorption of surface hydroxyls, but to the recombinative desorption of Ce^{4+}–H^- species as H_2. Corresponding results of water adsorbed on the CeO_{2-x} powder (Figure S9) show that molecular water desorption mainly occurs before 450 K, consistent with the TDS observations.

While CeO_{2-x}(111) thin films and CeO_{2-x} powders are significantly different in their morphology and defect density, we see a remarkable agreement in the thermal stability of the observed hydride species. In both systems, the Ce^{3+} concentration is (partially) recovered upon heating to 450 K.

According to our results, we suggest the following description of the adsorption of H_2 at Ce^{3+}/oxygen vacancy sites ($Ce^{3+}{}_{Vo}$) and the corresponding recombinative desorption. Please note that these are net equations, and that intermediate steps may occur.

$$H_2 + 2\,Ce^{3+}{}_{Vo} \xrightarrow{RT} 2\,Ce^{4+}{}_{Vo}\text{–}H^- \quad (2)$$

$$2\,Ce^{4+}{}_{Vo}\text{–}H^- \xrightarrow{\Delta,\ \approx 450\,K} H_2 + 2\,Ce^{3+}{}_{Vo} \quad (3)$$

At RT, H_2 dissociates at $Ce^{3+}{}_{Vo}$ sites to form $Ce^{4+}{}_{Vo}$–H^- hydride species, oxidizing the $Ce^{3+}{}_{Vo}$ species to $Ce^{4+}{}_{Vo}$. Upon heating, $Ce^{4+}{}_{Vo}$–H^- species recombine and desorb as H_2, which recovers the $Ce^{3+}{}_{Vo}$ oxidation state.

The interaction of H_2 with CeO_2 has been intensely studied by DFT calculations.[12f,h,13,14] The interaction of H_2 and oxygen vacancy sites, however, has not yet been fully explored. DFT calculation results [12h] show that H_2 adsorbs at a surface oxygen vacancy site of the CeO_2(111) surface (oxygen vacancy concentration: 1.85%) with an adsorption energy of −0.19 eV ($H_2 + Vo \rightarrow H_2$*) and that its heterolytic dissociation to OH and Ce–H species is exothermic (H_2*→ H*-O + H*-Ce, $E = -0.56$ eV) and proceeds with an activation barrier of 0.52 eV. The transformation of CeH species

into OH species, although exothermic (H*-Ce→H*-O, $E = -1.47$ eV), needs to overcome a barrier of 1.64 eV. From these data, we calculated that the dissociation of H_2 on the $CeO_2(111)$ surface with an oxygen vacancy concentration of 1.85% to form two Ce–H hydride species is endothermic ($E = 0.72$ eV). However, the hydride species on an oxide surface is more stabilized as the oxygen vacancy concentration increases.[11a] Therefore, under our experimental conditions of high-pressure H_2 interaction with CeO_{2-x} samples at RT, the observed oxidation by the overwhelming formation of CeH species should be likely. Meanwhile, the recombinative reaction of OH and CeH species to H_2, although endothermic ($E = 0.56$ eV), only needs to overcome a barrier of 1.08 eV. This implies that the recombinative reaction of the $Ce^{4+}{}_{Vo}$-H^- species to H_2 should be kinetically favored over its transformation into OH species.

Conclusion

Via a comprehensive study of H_2 adsorption on reduced $CeO_{2-x}(111)$ thin films and CeO_{2-x} powders at room temperature, we have provided insights into a novel mechanism of hydrogen adsorption within ceria. In the presence of oxygen vacancies, H species may bind to $Ce^{3+}{}_{Vo}$ sites in the form of hydrides. The formation of a hydride species, $Ce^{4+}{}_{Vo}$–H^-, is achieved via electron transfer from $Ce^{3+}{}_{Vo}$ to hydrogen, thereby oxidizing Ce^{3+} to Ce^{4+}. At the same time, the valence structure of fully oxidized CeO_2 is recovered. Upon heating, $Ce^{4+}{}_{Vo}$–H^- species recombine to desorb as H_2, while the $Ce^{3+}{}_{Vo}$ sites, and thereby the initial oxidation state, are recovered. The observed desorption of H_2 is not related to desorption of surface hydroxyls.

These results not only broaden our fundamental understandings of elementary surface reactions of H_2 on oxide surfaces, but also demonstrate the powerful approach of combining well-defined single crystal model systems and corresponding powder systems in fundamental studies. The reactivity of the $Ce^{4+}{}_{Vo}$–H^- species, particularly in hydrogenation reactions, is currently under investigation in our laboratory.

Experimental Section

Powder studies were performed on commercial CeO_2 powder (Sigma Aldrich, Ref. 700290). Experiments on the powder samples were carried out with H_2, He and Ar (purity >99.999%, Nanjing Shangyuan Industrial Factory) and D_2 (purity >99.99%, Suzhou Changyou Gas Co., Ltd.).

TEM and HRTEM images of ceria powder were recorded on JEOL-2010 and JEOL-2100F setups at an electron acceleration voltage of 200 kV. XRD patterns were recorded on a Philips X'Pert Pro Super diffractometer, with a Cu Kα radiation ($\lambda = 0.15418$ nm) source, operating at 40 kV and 50 mA.

XPS measurements of ceria powders were carried out on a Thermo Scientific Escalab 250Xi setup, equipped with an ambient-pressure preparation chamber, using an Al Kα ($h\nu = 1486.6$ eV) source. Reference spectra of the powder were obtained at room temperature after pretreatment at 773 K in vacuum for 30 min. Then the sample was transferred to the preparation chamber, heated in 1 atm H_2 at desired temperatures for 1 h, and cooled in H_2 to room temperature. XP spectra were measured after transfer to the analysis chamber in vacuum. Further spectra were obtained after subsequent annealing at a desired temperature for 1 h, and cooling to room temperature.

Synchrotron radiation photoelectron spectroscopy (SREPS) of ceria powder was performed on the photoelectron spectroscopy endstation of the BL10B beamline in the National Synchrotron Radiation Laboratory (Hefei, China), which is equipped with a high-pressure preparation chamber. The beamline is connected to a bending magnet and equipped with three gratings that cover photon energies from 100 to 1000 eV with a typical photon flux of 1×10^{10} photons s^{-1} and a resolution ($E/\Delta E$) better than 1000. The analysis chamber connected to the beamline is equipped with a VG Scienta R3000 electron energy analyzer for SRPES measurements. A reference spectrum was obtained after pretreatment at 773 K in vacuum for 30 min and subsequent cooling. Then the sample was transferred into the preparation chamber, heated in 10 atm H_2 at 773 K for 1 h, and subsequently cooled to room temperature. SRPES measurements of the H_2-treated powder were obtained after transfer in vacuum to the analysis chamber. Further spectra were obtained after subsequent annealing at various temperatures. Ce 3d, O 1s, and C 1s XPS spectra were measured using a Mg Kα ($h\nu = 1253.6$ eV) source, and valence band spectra in the Ce 4d-4f photon absorption region were measured with photons of 124.5 and 122 eV for on-resonance spectra and of 115 eV for off-resonance spectra.

To record TDS curves, 100 mg ceria powder were placed in a high-pressure stainless steel tube, pretreated at 773 K for 2 h in He (flow rate 30 mL min^{-1}), and then cooled to 303 K. The gas stream was switched to H_2 with a flow rate of 30 mL min^{-1} at the desired pressures. The powder was heated to the desired temperatures at a heating rate of 10 K min^{-1} and kept there for 1 h. Then the powder was cooled to 303 K, purged in He, and heated to 773 K (10 K min^{-1}), during which the H_2 and H_2O signals were monitored to give corresponding TDS data.

The high-pressure stainless steel tube was equipped with two valves that were closed to seal the powder sample from ambient atmosphere. After H_2 treatment and cooling to 303 K (in H_2 or He), the tube was sealed and re-opened in an Ar-filled glovebox (Mikrouna Co. Ltd., China, O_2 concentrations below 0.1 ppm), wherein 120 mg of the powder sample were sealed into an electron spin resonance (ESR) sample tube. ESR spectra were recorded at 140 K on a JEOL JES-FA200 ESR spectrometer (9.087 GHz) at a microwave power of 0.998 mW, a modulation frequency of 100 kHz, and a modulation amplitude of 0.35 mT.

$CeO_{2-x}(111)$ thin film preparation, H_2 treatment, and corresponding XPS and EELS measurements were performed in two UHV systems with a base pressure of $\approx 1 \times 10^{-10}$ mbar, which are described in detail elsewhere.[17,30] Following an established recipe,[17] a ≈6–10 nm thick film of stoichiometric $CeO_2(111)$ was prepared on a Ru(0001) substrate (MaTeck) by molecular beam epitaxy in an O_2-rich environment. To prepare the reduced $CeO_{2-x}(111)$ thin film, the stoichiometric $CeO_2(111)$ film was annealed at 1200 K for 20 min. Before any experiment, the sample was flashed to 650 K to desorb surface impurities (especially adsorbed water from residual gas). The film was exposed to D_2 (Linde, purity 99.999%) or H_2 (Linde, purity 99.9999%) at 10 mbar for 15 min in the preparation chamber and then transferred to the analysis chamber in vacuum. Possible traces of water in the gas handling lines were eliminated by use of a cold trap (liquid N_2).

LEED was performed on a Specs ErLEEED 1000-A setup. XP spectra of $CeO_{2-x}(111)$ thin films were recorded using an Al Kα (Specs XR 50, $h\nu = 1486.6$ eV) source and a hemispherical analyzer (Specs Phoibos 150 MCD, pass energy 20 eV). EELS data were recorded with a Delta 0.5 spectrometer manufactured by VSW. The electron incidence angle with respect to the surface normal was set to 60° and the energy of the electron beam was 46 eV.

Acknowledgements

We thank the National Key R & D Program of MOST (2017YFB0602205), the DFG-NSFC joint project (Nos. FR554/18-1 and 21761132005), the National Natural Science Foundation of China (21525313, 91745202) and the Changjiang Scholars Program of Ministry of Education of China for financial support.

Conflict of interest

The authors declare no conflict of interest.

Stichwörter: Ceroxid · Hydride · Oxidation · Pulver · Dünne Filme

Zitierweise: *Angew. Chem. Int. Ed.* **2019**, *58*, 14686 – 14693
Angew. Chem. **2019**, *131*, 14828 – 14835

[1] R. Más-Balleste, A. Lledós in *Comprehensive Inorganic Chemistry II: From Elements to Applications*, *Vol. 9* (Eds.: J. Reedijk, K. Poeppelmeier), Elsevier, Oxford, **2013**, p. 727.
[2] a) V. E. Henrich, P. A. Cox, *The Surface Science of Metal Oxides*, Cambridge University Press, Cambridge, **1994**, p. 247; b) J. L. G. Fierro, *Metal Oxides: Chemistry and Applications*, CRC Press, Boca Raton, **2006**.
[3] C. Copéret, D. P. Estes, K. Larmier, K. Searles, *Chem. Rev.* **2016**, *116*, 8463 – 8505.
[4] a) E. N. Gribov, S. Bertarione, D. Scarano, C. Lamberti, G. Spoto, A. Zecchina, *J. Phys. Chem. B* **2004**, *108*, 16174 – 16186; b) H.-Y. T. Chen, L. Giordano, G. Pacchioni, *J. Phys. Chem. C* **2013**, *117*, 10623 – 10629.
[5] J. Joubert, A. Salameh, V. Krakoviack, F. Delbecq, P. Sautet, C. Copéret, J. M. Basset, *J. Phys. Chem. B* **2006**, *110*, 23944 – 23950.
[6] D. Martin, D. Duprez, *J. Phys. Chem. B* **1997**, *101*, 4428 – 4436.
[7] a) C. Binet, M. Daturi, J.-C. Lavalley, *Catal. Today* **1999**, *50*, 207 – 225; b) H.-T. Chen, Y. M. Choi, M. Liu, M. C. Lin, *ChemPhysChem* **2007**, *8*, 849 – 855; c) M. Menetrey, A. Markovits, C. Minot, *Surf. Sci.* **2003**, *524*, 49 – 62.
[8] P. Meriaudeau, M. Primet, *J. Mol. Catal.* **1990**, *61*, 227 – 234.
[9] G. Busca, *J. Catal.* **1989**, *120*, 303 – 313.
[10] a) R. P. Eischens, W. A. Pliskin, M. J. D. Low, *J. Catal.* **1962**, *1*, 180 – 191; b) A. L. Dent, R. J. Kokes, *J. Phys. Chem.* **1969**, *73*, 3781 – 3790; c) T. Becker, S. Hövel, M. Kunat, C. Boas, U. Burghaus, C. Wöll, *Surf. Sci.* **2001**, *486*, L502 – L506.
[11] a) Z. Wu, W. Zhang, F. Xiong, Q. Yuan, Y. Jin, J. Yang, W. Huang, *Phys. Chem. Chem. Phys.* **2014**, *16*, 7051 – 7057; b) Z. Wu, F. Xiong, Z. Wang, W. Huang, *Chin. Chem. Lett.* **2018**, *29*, 752 – 756.
[12] a) G. Vilé, B. Bridier, J. Wichert, J. Pérez-Ramírez, *Angew. Chem. Int. Ed.* **2012**, *51*, 8620 – 8623; *Angew. Chem.* **2012**, *124*, 8748 – 8751; b) J. Carrasco, G. Vilé, D. Fernández-Torre, R. Pérez, J. Pérez-Ramírez, M. V. Ganduglia-Pirovano, *J. Phys. Chem. C* **2014**, *118*, 5352 – 5360; c) G. Vilé, S. Wrabetz, L. Floryan, M. E. Schuster, F. Girgsdies, D. Teschner, J. Pérez-Ramírez, *ChemCatChem* **2014**, *6*, 1928 – 1934; d) G. Vilé, P. Dähler, J. Vecchietti, M. Baltanás, S. Collins, M. Calatayud, A. Bonivardi, J. Pérez-Ramírez, *J. Catal.* **2015**, *324*, 69 – 78; e) G. Vilé, S. Colussi, F. Krumeich, A. Trovarelli, J. Pérez-Ramírez, *Angew. Chem. Int. Ed.* **2014**, *53*, 12069 – 12072; *Angew. Chem.* **2014**, *126*, 12265 – 12268; f) M. García-Melchor, L. Bellarosa, N. López, *ACS Catal.* **2014**, *4*, 4015 – 4020; g) S. Zhang, Z.-Q. Huang, Y. Ma, W. Gao, J. Li, F. Cao, L. Li, C.-R. Chang, Y. Qu, *Nat. Commun.* **2017**, *8*, 15266; h) C. Riley, S. Zhou, D. Kunwar, A. De La Riva, E. Peterson, R. Payne, L. Gao, S. Lin, H. Guo, A. Datye, *J. Am. Chem. Soc.* **2018**, *140*, 12964 – 12973; i) T. Cao, R. You, X. Zhang, S. Chen, D. Li, Z. Zhang, W. Huang, *Phys. Chem. Chem. Phys.* **2018**, *20*, 9659 – 9670.
[13] a) D. Fernández-Torre, J. Carrasco, M. V. Ganduglia-Pirovano, R. Pérez, *J. Chem. Phys.* **2014**, *141*, 014703; b) F. R. Negreiros, M. F. Camellone, S. Fabris, *J. Phys. Chem. C* **2015**, *119*, 21567 – 21573; c) M. García-Melchor, N. López, *J. Phys. Chem. C* **2014**, *118*, 10921 – 10926.
[14] Z.-Q. Huang, L.-P. Liu, S. Qi, S. Zhang, Y. Qu, C.-R. Chang, *ACS Catal.* **2018**, *8*, 546 – 554.
[15] a) B. Chen, Y. Ma, L. Ding, L. Xu, Z. Wu, Q. Yuan, W. Huang, *J. Phys. Chem. C* **2013**, *117*, 5800 – 5810; b) Y. Gao, R. Li, S. Chen, L. Luo, T. Cao, W. Huang, *Phys. Chem. Chem. Phys.* **2015**, *17*, 31862 – 31871.
[16] Z. Wu, Y. Cheng, F. Tao, L. Daemen, G. S. Foo, L. Nguyen, X. Zhang, A. Beste, A. J. Ramirez-Cuesta, *J. Am. Chem. Soc.* **2017**, *139*, 9721 – 9727.
[17] K. Werner, X. Weng, F. Calaza, M. Sterrer, T. Kropp, J. Paier, J. Sauer, M. Wilde, K. Fukutani, S. Shaikhutdinov, H.-J. Freund, *J. Am. Chem. Soc.* **2017**, *139*, 17608 – 17676.
[18] F. Dvořák, L. Szabová, V. Johánek, M. Farnesi Camellone, V. Stetsovych, M. Vorokhta, A. Tovt, T. Skála, I. Matolínová, Y. Tateyama, J. Mysliveček, S. Fabris, V. Matolín, *ACS Catal.* **2018**, *8*, 4354 – 4363.
[19] a) R. Olbrich, G. E. Murgida, V. Ferrari, C. Barth, A. M. Llois, M. Reichling, M. V. Ganduglia-Pirovano, *J. Phys. Chem. C* **2017**, *121*, 6844 – 6851; b) T. Duchoň, F. Dvořák, M. Aulická, V. Stetsovych, M. Vorokhta, D. Mazur, K. Veltruská, T. Skála, J. Mysliveček, I. Matolínová, V. Matolín, *J. Phys. Chem. C* **2014**, *118*, 357 – 365; c) T. Duchoň, F. Dvořák, M. Aulická, V. Stetsovych, M. Vorokhta, D. Mazur, K. Veltruská, T. Skála, J. Mysliveček, I. Matolínová, V. Matolín, *J. Phys. Chem. C* **2014**, *118*, 5058 – 5059; d) H. Wilkens, O. Schuckmann, R. Oelke, S. Gevers, A. Schaefer, M. Bäumer, M. H. Zoellner, T. Schroeder, J. Wollschläger, *Appl. Phys. Lett.* **2013**, *102*, 111602; e) D. C. Grinter, C. Muryn, A. Sala, C.-M. Yim, C. L. Pang, T. O. Menteş, A. Locatelli, G. Thornton, *J. Phys. Chem. C* **2016**, *120*, 11037 – 11044.
[20] S. Tanuma, C. J. Powell, D. R. Penn, *Surf. Interface Anal.* **1993**, *20*, 77 – 89.
[21] Y. Lykhach, S. M. Kozlov, T. Skála, A. Tovt, V. Stetsovych, N. Tsud, F. Dvořák, V. Johánek, A. Neitzel, J. Mysliveček, S. Fabris, V. Matolín, K. M. Neyman, J. Libuda, *Nat. Mater.* **2015**, *15*, 284 – 289.
[22] Y. Lykhach, V. Johánek, H. A. Aleksandrov, S. M. Kozlov, M. Happel, T. Skála, P. S. Petkov, N. Tsud, G. N. Vayssilov, K. C. Prince, K. M. Neyman, V. Matolín, J. Libuda, *J. Phys. Chem. C* **2012**, *116*, 12103 – 12113.
[23] a) A. Laachir, V. Perrichon, A. Badri, J. Lamotte, E. Catherine, J. C. Lavalley, J. El Fallah, L. Hilaire, F. Le Normand, E. Quemere, G. N. Sauvion, O. Touret, *J. Chem. Soc. Faraday Trans.* **1991**, *87*, 1601 – 1609; b) P. Ernesto, *J. Phys. Condens. Matter* **2018**, *30*, 343003.
[24] a) J. Paier, C. Penschke, J. Sauer, *Chem. Rev.* **2013**, *113*, 3949 – 3985; b) S. Fabris, G. Vicario, G. Balducci, S. de Gironcoli, S. Baroni, *J. Phys. Chem. B* **2005**, *109*, 22860 – 22867; c) Z. Yang, T. K. Woo, M. Baudin, K. Hermansson, *J. Chem. Phys.* **2004**, *120*, 7741 – 7749.
[25] J. Höcker, T. O. Menteş, A. Sala, A. Locatelli, T. Schmidt, J. Falta, S. D. Senanayake, J. I. Flege, *Adv. Mater. Interfaces* **2015**, *2*, 1500314.
[26] S. Vangelista, R. Piagge, S. Ek, T. Sarnet, G. Ghidini, C. Martella, A. Lamperti, *Thin Solid Films* **2017**, *636*, 78 – 84.

[27] E. Abi-aad, R. Bechara, J. Grimblot, A. Aboukais, *Chem. Mater.* **1993**, *5*, 793 – 797.
[28] J. A. Weil, J. R. Bolton, *Electron Paramagnetic Resonance: Elementary Theory and Practical Applications*, Wiley, Hoboken, **2007**, pp. 73 – 74.
[29] A. Pfau, K. D. Schierbaum, *Surf. Sci.* **1994**, *321*, 71 – 80.
[30] N. F. Richter, F. E. Feiten, J. Pal, A. Płucienik, E. Emmez, S. Shaikhutdinov, H. Kuhlenbeck, T. Risse, H.-J. Freund, I. Goikoetxea, R. Włodarczyk, J. Sauer, *J. Phys. Chem. C* **2019**, *123*, 7110 – 7117.

Manuskript erhalten: 7. Juni 2019
Veränderte Fassung erhalten: 8. Juli 2019
Akzeptierte Fassung online: 12. August 2019
Endgültige Fassung online: 12. September 2019

